ACS APPLIED MATERIALS & INTERFACES

Expanded $MoSe_2$ Nanosheets Vertically Bonded on Reduced Graphene Oxide for Sodium and Potassium-Ion Storage

Shaokun Chong,* Xuedong Wei, Yifang Wu, Lan Sun, Chengyong Shu, Qianbo Lu, Yingzhen Hu, Guozhong Cao,* and Wei Huang*

Cite This: ACS Appl. Mater. Interfaces 2021, 13, 13158−13169

Read Online

ACCESS | Metrics & More | Article Recommendations | Supporting Information

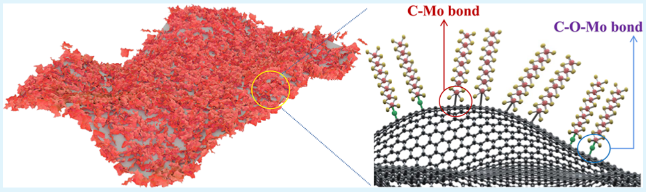

ABSTRACT: The cost-efficient and plentiful Na and K resources motivate the research on ideal electrodes for sodium-ion batteries (SIBs) and potassium-ion batteries (PIBs). Here, $MoSe_2$ nanosheets perpendicularly anchored on reduced graphene oxide (rGO) are studied as an electrode for SIBs and PIBs. Not only does the graphene network serves as a nucleation substrate for suppressing the agglomeration of $MoSe_2$ nanosheets to eliminate the electrode fracture but also facilitates the electrochemical kinetics process and provides a buffer zone to tolerate the large strain. An expanded interplanar spacing of 7.9 Å is conducive to fast alkaline ion diffusion, and the formed chemical bondings (C−Mo and C−O−Mo) promote the structure integrity and the charge transfer kinetics. Consequently, $MoSe_2$@5%rGO exhibits a reversible specific capacity of 458.3 $mAh \cdot g^{-1}$ at 100 $mA \cdot g^{-1}$, great cyclability with a retention of 383.6 $mAh \cdot g^{-1}$ over 50 cycles, and excellent rate capability (251.3 $mAh \cdot g^{-1}$ at 5 $A \cdot g^{-1}$) for SIBs. For PIBs, a high first specific capacity of 365.5 $mAh \cdot g^{-1}$ at 100 $mA \cdot g^{-1}$ with a low capacity fading of 51.5 $mAh \cdot g^{-1}$ upon 50 cycles and satisfactory rate property are acquired for $MoSe_2$@10%rGO composite. *Ex situ* measurements validate that the discharge products are Na_2Se for SIBs and K_5Se_3 for PIBs, and robust chemical bonds boost the structure stability for Na- and K-ion storage. The full batteries are successfully fabricated to verify the practical feasibility of $MoSe_2$@5%rGO composite.

KEYWORDS: *sodium-ion battery, potassium-ion battery, anode material, chemical bond, molybdenum selenide*

1. INTRODUCTION

Nowadays, the exhaustion of nonrenewable natural resources and the worsening of the environment promote the development of advanced energy storage (EES) devices to match smart electric grids by integrating renewable energy.[1,2] On the basis of high power density, large energy density, and satisfactory cycling life, the market for portable electronic devices (PEDs) and electric vehicles (EVs) is dominated by rechargeable lithium-ion batteries (LIBs).[3−5] However, the uneven geographical distribution and limited reserve of lithium seriously humble LIBs' widespread applications for the increasing demands for PEDs, EVs, and stationary EES technologies, which urges for the investigation on new rechargeable alkaline ion batteries with abundant resources.[3] Hence, sodium-ion batteries (SIBs) and potassium-ion batteries (PIBs), as promising alternatives to LIBs, have been widely concerned and studied.[6,7] It is a key challenge to search innovative electrodes for storing large-sized Na ions (1.02 Å) and K ions (1.38 Å) to promote the advance of SIBs and PIBs. The study on cathode materials, including layered oxides, organic materials, Prussian blue analogues, and polyanionic compounds, has made great progress in a detailed electrochemical reaction process and performances for both SIBs and PIBs.[8−11]

For the anode materials, although the commercialized graphite electrode can store K ions to form KC_8 with a low specific capacity of 279 $mAh \cdot g^{-1}$, it is thermodynamically unfavorable to generate a binary graphite intercalation compound for Na-ion storage.[12,13] Even for the silicon anode with ultrahigh theoretical specific capacity in LIBs, there is no experimental evidence to confirm the successful insertion/extraction of Na and K ions in the silicon host.[14−16] The amorphous carbon delivers more capacity induced by nanovoids and defects than graphite, while ultralow initial Coulombic efficiency is obtained owing to a more irreversible product resulted from the exposed edge planes.[17,18] So far, the materials based on the alloying−dealloying mechanism, such as phosphorus (P), tin (Sn), antimony (Sb), bismuth (Bi), germanium (Ge), and lead (Pb), deliver satisfactory high specific capacity, yet the resulting large volume change leads to poor cyclic stability.[13,19] Another type of anode materials based on conversion mechanism exhibit a satisfactory combination of

Received: December 18, 2020
Accepted: March 8, 2021
Published: March 14, 2021

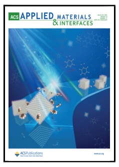

https://dx.doi.org/10.1021/acsami.0c22430

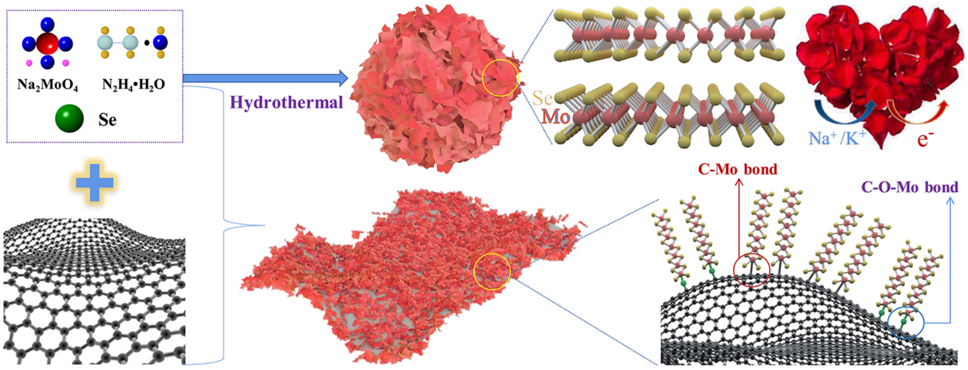

Figure 1. Graphic illustration of the assembly procedure of $MoSe_2$ and hierarchical $MoSe_2$@rGO composite.

high capacity and relatively smaller volume variation, prompting the study on transition metal (TM) oxides, sulfides, selenides, nitrides, phosphides, carbides, etc.[7,20−22]

Layered TM dichalcogenides, possessing a narrow band gap semiconductor characteristic, considerable interlayer spacing, and two-dimensional (2D) lamellar structure, are widely applied as promising anode electrodes for efficient energy storage.[23−26] Especially, molybdenum diselenide ($MoSe_2$) is regarded as an emerging valuable anode for Na- and K-ion storage owing to its intrinsic sandwich-like structure, which is constructed by forming a Mo-Se monolayer via a strong in-plane covalent bond and further stacking of the neighboring layers via weak van der Waals force.[27] In addition, the greater interlayer distance (6.4 Å) and smaller band gap (1.1 eV) facilitate efficient electron transfer and ion transport.[28,29] However, several key issues of $MoSe_2$ are the nanosheet agglomeration during synthesis caused by the high surface energy of the 2D nanostructure, large volume change upon ion insertion/extraction process, and electrical conductivity that need to be improved, which will give rise to poor cycling stability and rate performance.[30,31] Therefore, it is vitally necessary to adopt a simple strategy that can not only suppress the stacking of nanosheets to prevent the electrode breakage caused by stress but also contribute a buffer zone to tolerate the volume variation and effectively improve the electrochemical dynamic process.

Herein, we constructed ultrathin $MoSe_2$ nanosheets perpendicularly confined into the surface of reduced graphene oxide (rGO) through a hydrothermal strategy as an anode for Na- and K-ion storage, where the composites with rGO mass contents of 1, 5, 10, and 20% are named $MoSe_2$@1%rGO, $MoSe_2$@5%rGO, $MoSe_2$@10%rGO, and $MoSe_2$@20%rGO, respectively. This unique heterogeneous composite, with a robust interfacial joint of C−Mo and C−O−Mo bonds and enlarged interlayer crystal distance of 7.9 Å in $MoSe_2$, is conducive to ensuring structural stability from the huge volume variation and acquire fast transportation capability of both electron and alkaline ions. Accordingly, a high specific capacity of 383.6 $mAh·g^{-1}$ upon 50 cycles at 100 $mA·g^{-1}$ and outstanding rate performance (251.3 $mAh·g^{-1}$ at 5 $A·g^{-1}$) can be achieved for the $MoSe_2$@5%rGO electrode as an anode for SIBs. In addition, $MoSe_2$@10%rGO delivers a reversible capacity of 365.5 $mAh·g^{-1}$ at 100 $mA·g^{-1}$, showing a high retention value of 314.0 $mAh·g^{-1}$ over 50 cycles and improved rate capability when it was tested for PIBs. It is demonstrated that both intercalation and conversion reactions play a part in alkaline ion storage, while the main discharge products are Na_2Se and K_5Se_3, respectively. We also successfully assembled the full cells based on the $Na_2Ni[Fe(CN)_6]$ or $K_2Ni[Fe(CN)_6]$ cathode and $MoSe_2$@5%rGO anode.

2. EXPERIMENTAL SECTION

2.1. Material Synthesis. Graphene oxide (GO) was synthesized through a modified Hummers' strategy. A series of $MoSe_2$@rGO composites were prepared by a simple hydrothermal approach. First, GO was dispersed into 25 mL of deionized water under a continuous sonication process, and 2 mmol $NaMoO_4·2H_2O$ was completely dissolved into the above solution and further mixed with 4 mmol Se powder in 10 mL of hydrazine hydrate. After that, the obtained uniform solution was moved to a 50 mL autoclave for the hydrothermal reaction at 200 °C with a holding time of 12 h in the oven. The powder was collected via washing with ethanol and ultrapure water under high-speed centrifugation as well as freeze-drying for 24 h. The pristine $MoSe_2$ was synthesized via the same method without GO. The additive amounts of GO for $MoSe_2$@1% rGO, $MoSe_2$@5%rGO, $MoSe_2$@10%rGO, and $MoSe_2$@20%rGO composites were 5.1, 26.7, 56.4, and 126.9 mg, respectively.

2.2. Material Characterization. The morphological and microstructural information of materials were analyzed via field-emission scanning electron microscopy (FESEM, JSM-6390) and transmission electron microscopy (TEM, JEOL JEM-2100CX). The elemental purity and distribution were identified through energy-dispersive X-ray spectrometry (EDS). X-ray diffraction (XRD) was conducted on Ultima IV-185 in which the detailed structural information was identified by the Rietveld method with program GSAS. Raman and thermogravimetry (TG) were carried out on a JY LabRAM spectrometer and TGA/DSC3+ instrument, respectively. A Micromeritics ASAP 2460 and Axis Ultra DLD spectrometer were employed to test N_2 adsorption−desorption and X-ray photoelectron spectroscopy (XPS), respectively.

2.3. Electrochemical Measurement. The electrochemical tests of alkaline ion storage for electrode materials were performed using Swagelok-type batteries in an Ar-filled glove box using a glass fiber as a separator. The counter electrodes for SIBs and PIBs are sodium and potassium metal sheets, respectively. The electrolytes for SIBs were $NaClO_4$ in diethyl carbonate, ethylene carbonate, and fluoroethylene carbonate (45:45:10 by volume ratio), and 1 M KPF_6 dissolved in propylene carbonate, diethyl carbonate, ethylene carbonate (1:1:1) were employed as the electrolytes for PIBs. The prepared active sample, Super P carbon black, and polyvinylidene fluoride (1:1:1 by mass ratio) were mixed in *N*-methyl-2-pyrrolidone to obtain the homogeneous slurry. The working electrode can be gained after coating the slurry on Cu foil, drying, and cutting into the disk. The batteries were measured on a CT2001A battery tester (Land) using galvanostatic charge/discharge tests in a potential range of 0.01−3.0 V (vs Na/Na^+ or vs K/K^+). A Solartron 1470E electrochemical potentiostat was utilized to test cyclic voltammetry (CV) at different sweep rates and electrochemical impedance spectroscopy (EIS). The Na-ion diffusion coefficient can be calculated via the galvanostatic intermittent titration technique (GITT) result, which was conducted

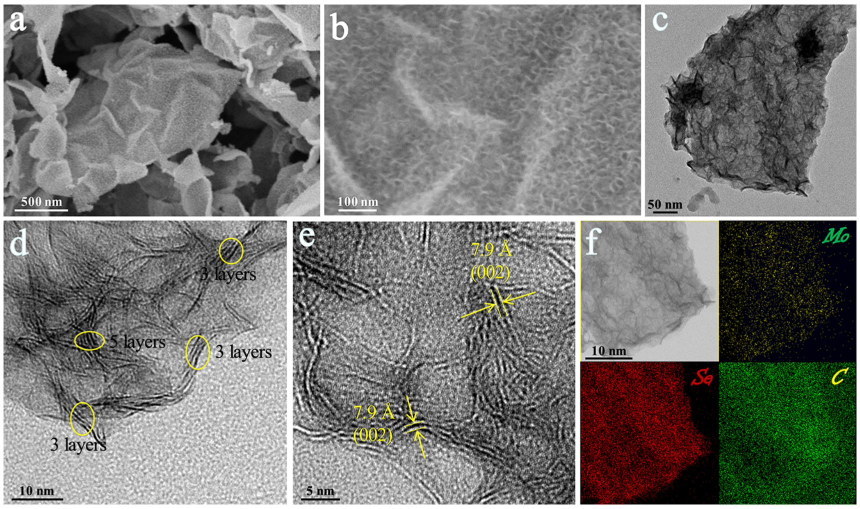

Figure 2. Morphology and structure characterization: (a, b) FESEM images at different magnifications, (c) TEM image, (d, e) HRTEM images, and (f) EDS mapping images of $MoSe_2$@5%rGO.

by galvanostatic charging/discharging for 600 s and an open circuit relaxation for 3600 s. The electrochemical reaction mechanism and morphology stability were investigated through measuring the samples at the initial full discharge/charge states, where the electrode was attained after disassembling the cell and washing the sample. The Na- and K-ion full cells were designed with a cathode/anode mass ratio of around 2:1 using $Na_2Ni[Fe(CN)_6]$ and $K_2Ni[Fe(CN)_6]$ cathodes, respectively, and the full batteries were tested within a potential window of 2.0−4.5 V.

3. RESULTS AND DISCUSSION

Figure 1 illustrates the preparation procedure of $MoSe_2$ and $MoSe_2$@rGO composites by a hydrothermal method using sodium molybdate as the Mo source and selenium powder as the Se source. Hydrazine hydrate plays the role in forming the hydrazine-Se and efficient reduction reaction of Se and MoO_4^{2-}. FESEM images of bare $MoSe_2$ display nanoflower morphology self-assembled by nanosheets in Figure S1. GO with rich surface functional groups acts as a 3D conductive network to induce the nucleation and growth of $MoSe_2$ nanosheets, thus causing the formation of C−Mo and C−O−Mo chemical bonds at the interface of heterostructures, which is in favor of accommodating huge volume expansion during the charge/discharge process. Therefore, ultrathin $MoSe_2$ nanosheets are vertically confined into the surface of rGO to produce a developed honeycomb-like hierarchical structure for composites as exhibited in Figure S2 ($MoSe_2$@1% rGO), Figure 2a,b ($MoSe_2$@5%rGO), and Figure S3 ($MoSe_2$@10%rGO), thus facilitating great kinetics behavior for fast electron and alkaline ion transfer.

The TEM image of $MoSe_2$ in Figure S4a shows a spherical flower-like structure constructed by numerous nanosheets, which will increase the alkaline ion diffusion path during the charge/discharge process and reduce the specific capacities at high rates. The corresponding high-resolution (HR) TEM image in Figure S4b exhibits that nanosheets possess a thickness above 4.5 nm with multistacked layers (≥7), whose interplanar distance of lattice fringe is measured to be 6.5 Å, which is consistent with the reported value of pristine $MoSe_2$ assigned to the (002) plane of a hexagonal phase.[22] Figure S4c reveals the EDS elemental mapping images in which both elements are overlapping, indicating that Mo and Se are homogeneously distributed throughout the $MoSe_2$ nanoflower. As presented in Figure 2c, $MoSe_2$@5%rGO depicts a hierarchical architecture, where rGO is uniformly covered via perpendicular appositional growth of $MoSe_2$ nanosheets. Therefore, the enhanced interfacial contact between both heterostructures will promote outstanding structure stability during repeated cycles. The selected area electron diffraction (SAED) pattern in Figure S5 gives distinct polycrystalline diffraction rings, which are indexed to the (100) and (110) planes of the $MoSe_2$ hexagonal structure. It can be seen from the HRTEM image in Figure 2d that there are few stacks of layered structures for $MoSe_2$@5%rGO, which confirms that the rGO conductive substrate is beneficial to restraining the restacking of $MoSe_2$ nanosheets. Also, an obvious expanded interlayer spacing of 7.9 Å probably derived from the pulling effect of chemical bonds, ascribed to the (002) plane, is acquired as displayed in Figure 2e, which is expected to accelerate alkaline ion insertion/extraction and further result in remarkable rate capability. The coexistence and homogeneous distribution of Mo and Se elements on the C substrate in Figure 2f further confirm that $MoSe_2$ nanosheets are anchored on the surface of rGO.

Figure 3a exhibits the Rietveld refined XRD pattern of pristine $MoSe_2$, where all peaks are identified as a hexagonal phase ($P6_3/mmc$ space group) without any impure phase, and two-phase coexistence of hexagonal $MoSe_2$ and hexagonal graphene can be proved by the Rietveld refinement XRD result of $MoSe_2$@5%rGO in Figure 3b.[32,33] The intensity of the (002) plane of $MoSe_2$ for composites is much weaker than that of pure $MoSe_2$ as displayed in Figure S6, indicating that the growth of nanosheets induced by graphene can effectively inhibit the restacking along the (002) plane, thus forming few-layered structures, which is in well agreement with the HRTEM result. In order to further gain insight into the structure information, the Raman spectra are collected in Figure S7. There are two distinguishing peaks located at 244 and 292 cm^{-1} for all materials, corresponding to out-of-plane (A_{1g}) and in-plane (E^1_{2g}) modes of 2H-$MoSe_2$, and the intensity for composites becomes weaker compared with $MoSe_2$ due to the inherent absorption difference between $MoSe_2$ and rGO.[32,34] Raman spectra also show two sharp peaks at 1335 cm^{-1} (D band) and 1605 cm^{-1} (G band), which are related to sp^3 and sp^2 hybrids of C atoms, respectively,

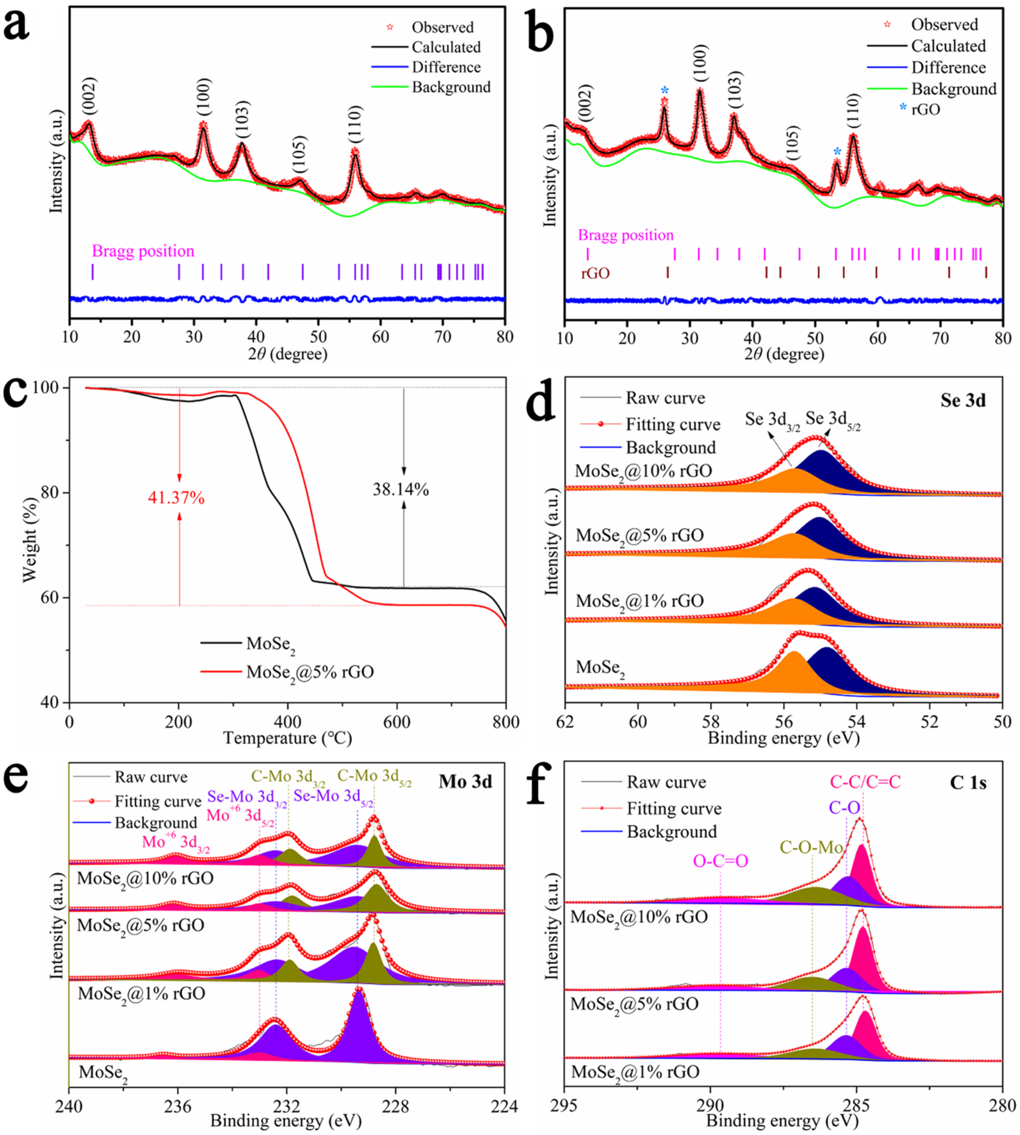

Figure 3. Structure characterization: Rietveld refinement XRD patterns of (a) $MoSe_2$ ($\chi^2 = 1.63$, $R_{wp} = 1.15\%$, and $R_p = 1.44\%$) and (b) $MoSe_2$@5%rGO ($\chi^2 = 1.38$, $R_{wp} = 2.25\%$, and $R_p = 1.70\%$); (c) TG curves of $MoSe_2$ and $MoSe_2$@5%rGO; (d) Se 3d XPS spectra and (e) Mo 3d spectra of $MoSe_2$, $MoSe_2$@1%rGO, $MoSe_2$@5%rGO, and $MoSe_2$@10%rGO; and (f) C 1s spectra of the three composites.

verifying the successful introduction of rGO.[35] The TG analysis curves of $MoSe_2$ and $MoSe_2$@5%rGO are displayed in Figure 3c, where the mass increase at around 300 °C is because of the oxidation reaction from $MoSe_2$ to MoO_3, and the following weight loss is resulted from the carbon oxidation and SeO_2 sublimation. Hence, the accurate content of $MoSe_2$ in $MoSe_2$@5%rGO can be calculated to be 94.8%, which is close to the designed experimental value. The N_2 adsorption−desorption isotherms of both materials indicate type IV curves with H4 hysteresis loops in Figure S8a, signifying a typical mesoporous structure, which is demonstrated by the mesoporous size distribution profiles (Figure S8b). Moreover, a higher BET specific surface area of 18.3 $m^2 \cdot g^{-1}$ is obtained for $MoSe_2$@5%rGO compared with that of 12.4 $m^2 \cdot g^{-1}$ for $MoSe_2$ attributable to the contribution of graphene.

The XPS survey spectra in Figure S9 reveal the existence of Se, Mo, C, and O elements in all composites. As presented in Figure 3d, the Se 3d spectra can be fitted into two peaks located at approximately 55.7 and 55.0 eV, which are related to Se $3d_{3/2}$ and Se $3d_{5/2}$, respectively, suggesting that an Se ion is negative bivalent.[29] In the high-resolution Mo 3d spectra (Figure 3e), there are two pairs of peaks located at 232.4, 229.4, 236.1, and 233.0 eV associated with Mo^{4+} $3d_{3/2}$ and Mo^{4+} $3d_{5/2}$ for $MoSe_2$ as well as Mo^{6+} $3d_{3/2}$ and Mo^{6+} $3d_{5/2}$ for MoO_3, respectively.[29−31] Furthermore, another two split peaks at 231.9 and 228.8 eV attributed to the Mo−C bond appear in Figure 3e for all composites, confirming the formation of chemical bond interaction at the interface of graphene and $MoSe_2$ nanosheets.[35−37] Figure 3f displays the C 1s spectra of all $MoSe_2$@rGO composites in which a novel peak of the Mo−O−C chemical bond can be seen at 286.5 eV except for 289.6 eV for O−C═O, 285.3 eV for C−O, and 284.8 eV for C−C/C═C.[35,38] The existence of chemical bonds can powerfully improve the interfacial stability and relieve the press from the large volume change during cycling.

The Na- and K-ion storage performances of all $MoSe_2$-based electrodes were assessed from 0.01 to 3.0 V. In order to investigate the redox process and electrochemical reversibility for SIBs, CV of $MoSe_2$@5%rGO is tested and exhibited in Figure 4a. It can be observed that there are five main peaks

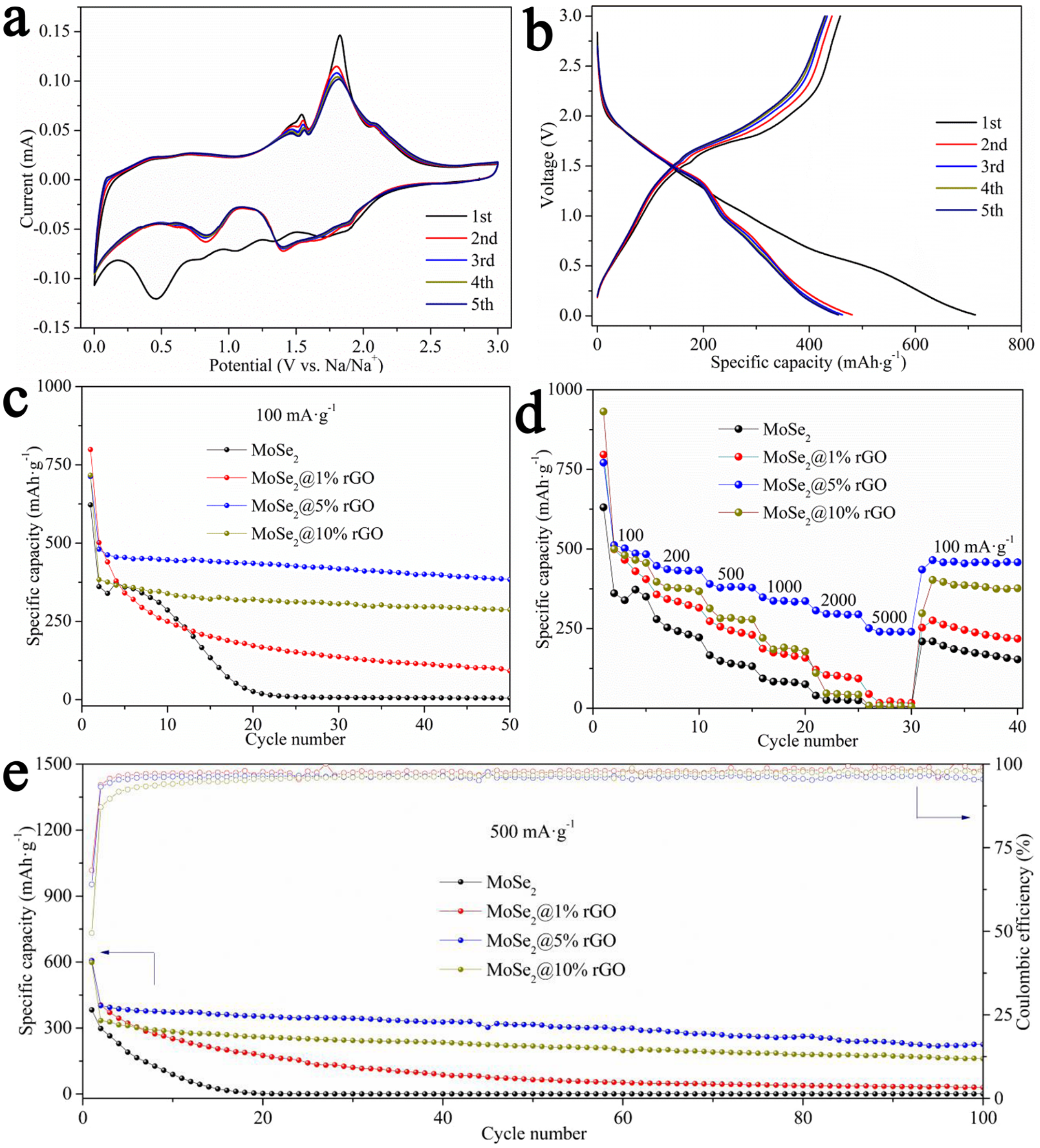

Figure 4. Electrochemical properties of SIBs: (a) CV and (b) charge/discharge curves of MoSe$_2$@5%rGO at 100 mA·g^{-1}; (c) cycling property at 100 mA·g^{-1}, (d) rate capability between 100 and 5000 mA·g^{-1}, and (e) cycling profiles of MoSe$_2$, MoSe$_2$@1%rGO, MoSe$_2$@5%rGO, and MoSe$_2$@10%rGO at 500 mA·g^{-1}.

during the initial discharge process, where the peaks located at 1.88, 1.35, and 0.80 V correspond to Na-ion insertion into the interlayers of MoSe$_2$ to generate Na$_x$MoSe$_2$ and further conversion into Mo and Na$_2$Se.[39] The peaks at 1.07 and 0.46 V are associated with the decomposition of the electrolyte and the formation of solid-state interphase (SEI) film.[39] Upon the following scans, the electrochemical processes occur reversibly, reflected by the redox peaks at 1.54/0.82, 1.82/1.41, and 2.08/1.90 V. Other three electrode materials show the similar redox behavior as exhibited in Figure S10. Figure 4b gives the galvanostatic charge/discharge curves of MoSe$_2$@5%rGO at 100 mA·g^{-1} in which the plateaus are well consistent with the CV result. The Na-ion insertion/extraction profiles are well overlapping after the first discharge, signifying highly reversible electrochemical behavior. The initial discharge/charge specific capacities of 622.3/338.1 mAh·g^{-1} (MoSe$_2$), 798.9/495.8 mAh·g^{-1} (MoSe$_2$@1%rGO), 712.7/458.3 mAh·g^{-1} (MoSe$_2$@5%rGO), and 716.9/355.2 mAh·g^{-1} (MoSe$_2$@10%rGO) can be achieved in Figure 4b and Figure S10. It can be found that MoSe$_2$@5%rGO shows the highest first Coulombic efficiency of 64.3%, which highlights the advantage of rGO to reduce the irreversible first capacity.

As displayed in Figure 4c, the cycling stability is gradually improved with the increase in rGO content, and the optimal electrochemical property is acquired for MoSe$_2$@5%rGO with the highest retention value of 383.6 mAh·g^{-1} over 50 cycles. The rate capability of all electrodes is presented in Figure 4d, where the highest capacities of 447.4, 390.0, 348.5, 306.9, and 251.3 mAh·g^{-1} at 200, 500, 1000, 2000, and 5000 mA·g^{-1} can be obtained, respectively, as well as the reversible capacity of 435.3 mAh·g^{-1} is maintained when the rate returns back to 100 mA·g^{-1} for MoSe$_2$@5%rGO. Table S1 and Figure S11 compare the rate properties of the ever reported MoSe$_2$-based anode materials for Na-ion storage in which MoSe$_2$@5%rGO in this work displays the best performance among them.[29,40−44] By comparing the corresponding charge/

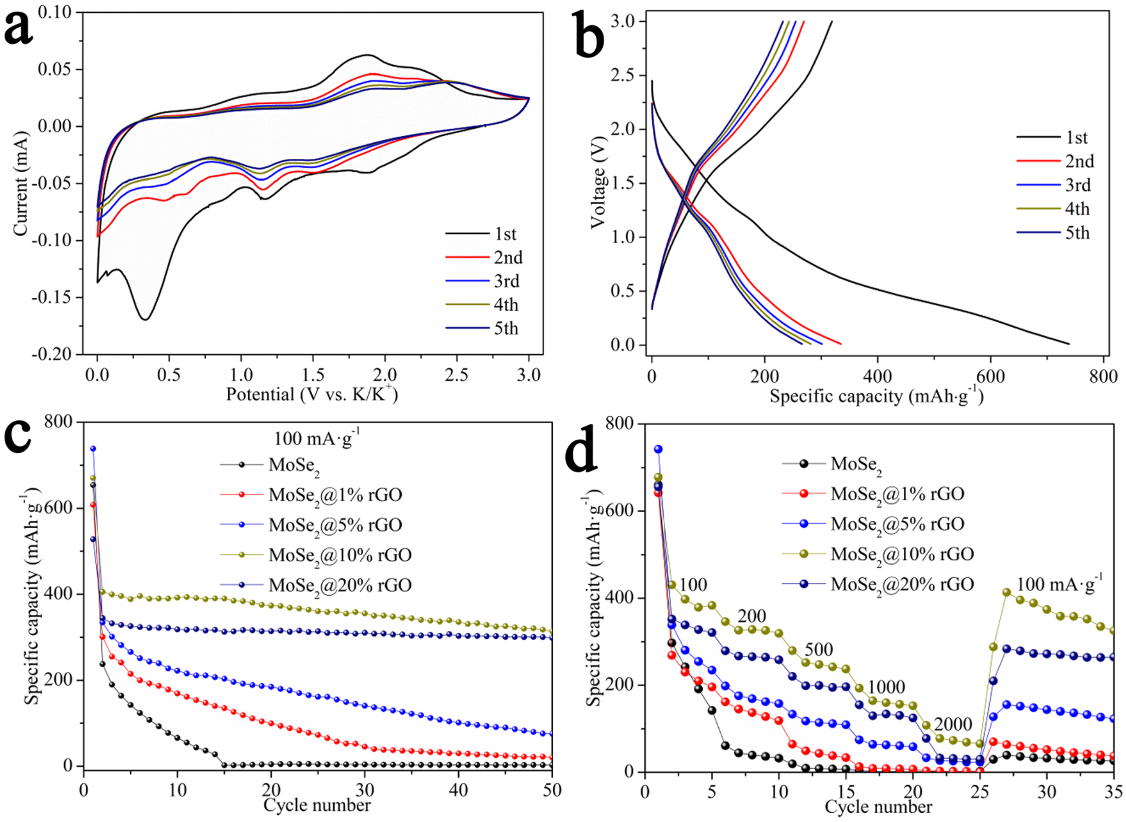

Figure 5. Electrochemical properties of PIBs: (a) CV and (b) charge/discharge profiles of $MoSe_2$@5%rGO at 100 mA·g^{-1}; (c) cycling property and (d) rate performance of pristine $MoSe_2$, $MoSe_2$@1%rGO, $MoSe_2$@5%rGO, $MoSe_2$@10%rGO, and $MoSe_2$@20%rGO between 100 and 2000 mA·g^{-1}.

discharge profiles at various rates in Figure S12, it can be found clearly that $MoSe_2$@5%rGO shows weaker polarization at high current density than pure $MoSe_2$, illuminating that outstanding electrochemical kinetics is responsible for the great rate performance. At 500 mA·g^{-1}, $MoSe_2$@5%rGO contributes a reversible second discharge capacity of 401.6 mAh·g^{-1} and great cyclic stability with a capacity of 225.3 mAh·g^{-1} over 100 cycles, while $MoSe_2$ suffers severe capacity fading from 297.8 to 0.6 mAh·g^{-1} in Figure 4e.

Figure 5a exhibits the CV profiles of $MoSe_2$@5%rGO for K-ion storage, presenting three peaks at 1.90, 1.16, and 0.33 V during the initial cathodic sweep, which are attributable to the partial reduction of $MoSe_2$ into K_xMoSe_2 via facile intercalation mechanism, reduction behavior based on the conversion process to form Mo and K_5Se_3, and irreversible decomposition of an electrolyte to produce the SEI film, respectively.[45] Two broad peaks at 1.85 and 2.23 V appear upon the first anodic scanning, which are related to the reversible conversion reaction from Mo metal to $MoSe_2$.[45] In the following sweeps, the oxidation/reduction couples can be stabilized at 1.91/1.16 and 2.45/1.54 V, which indicates excellent electrochemical reversibility and stability. However, the oxidation peak progressively shifts to higher voltage for pristine $MoSe_2$ in Figure S13a, revealing serious polarization phenomenon and poor electrochemical kinetics. By comparison, the intensity of redox peaks progressively becomes strong with the increase in graphene as presented in Figure 5a and Figures S14a, S15a, and S16a, suggesting that the introduction of graphene can give full play to the electrochemical activity of $MoSe_2$. The charge/discharge curves for $MoSe_2$@5%rGO at 100 mA·g^{-1} in Figure 5b present a distinct sloping voltage platform, which is in well agreement with the CV result. $MoSe_2$@5%rGO exhibits higher first discharge/charge capacities of 738.7/318.8 mAh·g^{-1} compared to those of 654.1/299.7 mAh·g^{-1} for pristine $MoSe_2$ (Figure S13b), 608.0/309.9 mAh·g^{-1} for $MoSe_2$@1%rGO (Figure S14b), and 527.8/312.8 mAh·g^{-1} for $MoSe_2$@20%rGO (Figure S16b). However, different from SIBs, $MoSe_2$@10%rGO shows the highest first Coulombic efficiency of 54.5% with discharge/charge capacities of 670.3/365.5 mAh·g^{-1} in Figure S15b, whose reversible charge capacity is higher than that of the published $MoSe_2$-based composites, such as $MoSe_2$/Mxene (350.0 mAh·g^{-1}) and $MoSe_2$/N−C (300.7 mAh·g^{-1}).[28,45] Also, it can be observed from Figure 5c that the increase in graphene will promote the enhancement of cyclic stability, which is similar with SIBs. Although the best cycling stability can be obtained for $MoSe_2$@20%rGO with a capacity of 298.4 mAh·g^{-1} upon 50 cycles, $MoSe_2$@10%rGO preserves the highest capacity of 314.0 mAh·g^{-1} compared with $MoSe_2$ (2.9 mAh·g^{-1}), $MoSe_2$@1%rGO (20.4 mAh·g^{-1}), and $MoSe_2$@5%rGO (75.7 mAh·g^{-1}). Also, $MoSe_2$@10%rGO composite exhibits much more superior rate property with high reversible capacities of 279.2, 220.4, 155.2, and 77.8 mAh·g^{-1} at 200, 500, 1000, and 2000 mA·g^{-1}, respectively, compared with other samples in Figure 5d. Therefore, $MoSe_2$@10%rGO exhibits the optimal K-ion storage performances by taking advantage of great kinetics and alleviating volume expansion effect from graphene and high capacity from $MoSe_2$.

Although $MoSe_2$@5%rGO presents satisfactory electrochemical properties in both Na- and K-ion storage, the cycling

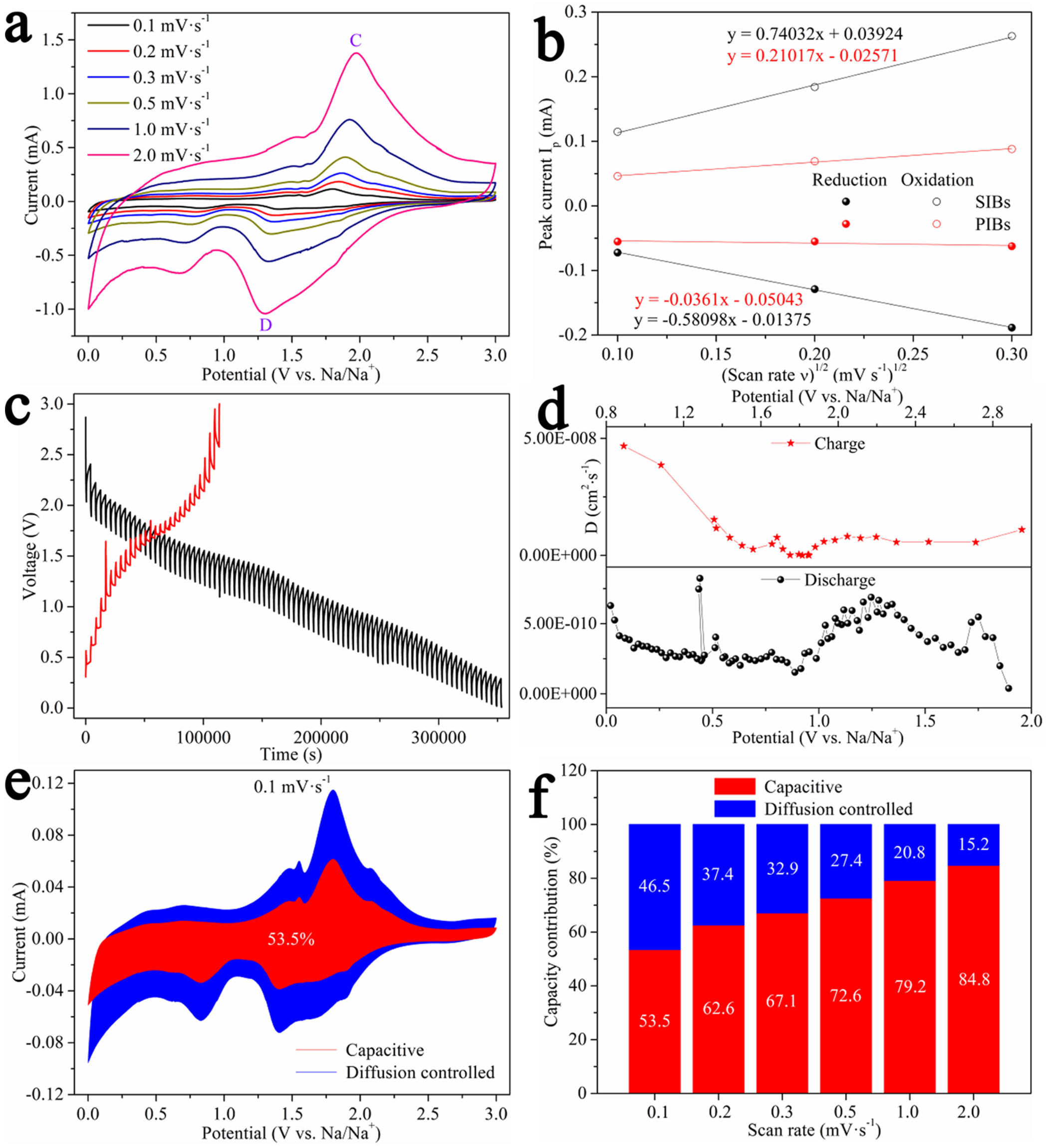

Figure 6. Electrochemical kinetics behavior: (a) CV curves at different sweep rates of MoSe$_2$@5%rGO for SIBs, (b) fitting linear relationship between I_p vs $v^{1/2}$ of MoSe$_2$@5%rGO for SIBs and PIBs; (c) GITT curve of MoSe$_2$@5%rGO at 100 mA·g^{-1} for SIBs and (d) calculated Na-ion diffusion coefficient; (e) CV curves at 0.1 mV·s^{-1} presenting the capacitive charge contribution, and (f) percentage of Na-ion diffusion and capacitive controlled at various sweep rates of MoSe$_2$@5%rGO.

stability and rate performance for SIBs are better than PIBs. Therefore, the electrochemical kinetics behavior is studied to clarify the detailed reasons. The CV profiles of MoSe$_2$@5%rGO for SIBs are exhibited in Figure 6a in which the analogue shapes can be maintained with the increase in scanning rates, illuminating more extraordinary response ability than PIBs (Figure S17). Randles–Sevcik equation of

$$I_p = 2.69 \times 10^5 n^{3/2} A D^{1/2} C v^{1/2} \tag{1}$$

can be utilized to calculate the alkaline ion diffusion coefficient (D), and I_p, n, A, C, and v are peak current, electron number, surface area of electrode, concentration of alkaline ion, and scan rate, respectively.[35,46] The D value can be represented by the slope of the fitting linear relationship of

$$I_p = a D^{1/2} v^{1/2} \tag{2}$$

between I_p and $v^{1/2}$ (a denoting the constant) in Figure 6b in which SIBs present much faster ion transfer capability than PIBs. The GITT in Figure 6c is further conducted at 100 mA·g^{-1} to calculate the exact solid-state diffusion coefficient of a Na ion, which is ascertained in the range of 3.9×10^{-11}–8.2×10^{-10} cm^2·s^{-1} for discharge and 1.7×10^{-12}–4.7×10^{-8} cm^2·s^{-1} for charge as displayed in Figure 6d. The EIS shows the decreasing trend of charge transfer resistance (R_{ct}) along with the increasing rGO amount for both SIBs and PIBs in Figure S18, manifesting that the existence of graphene can efficiently enhance the ion and electron transport. Also, R_{ct} values of all samples for SIBs are consistently lower than those for PIBs, which further verify more excellent electrochemical kinetics behavior for Na-ion storage, in accordance with the CV result.

The equation of

$$i = k_1 v + k_2 v^{1/2} \tag{3}$$

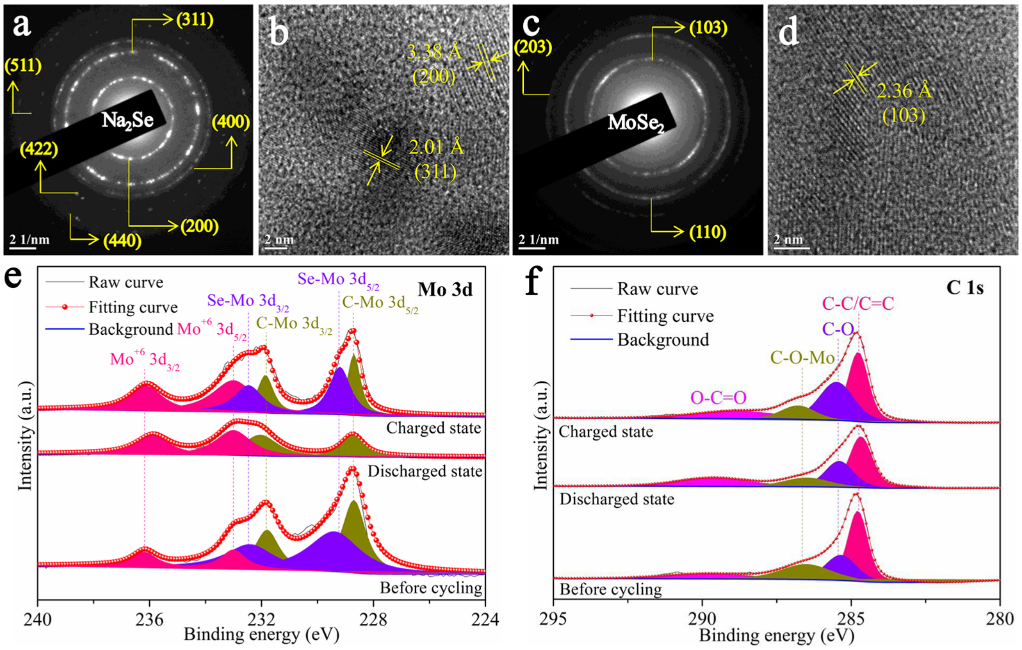

Figure 7. Na-ion storage mechanism of $MoSe_2$@5%rGO: SAED patterns and HRTEM images at the first fully (a,b) discharged and (c,d) charged states; (e) fitting Mo 3d XPS spectra and (f) C 1s spectra at different Na-ion insertion and extraction states.

describes the relationship between the current response (i) at a given potential and sweep rate (v), which can be further simplified as[23,35]

$$i/v^{1/2} = k_1 v^{1/2} + k_2. \tag{4}$$

Thus, the capacitance ($k_1 v$) and ionic diffusion ($k_2 v^{1/2}$) can be calculated through determining the values of k_1 and k_2 after fitting the linear relationship between $i/v^{1/2}$ and $v^{1/2}$. It can be observed from Figure 6e that the total charge is dominated by the capacitive effect (53.5%) at 0.1 mV·s^{-1}, and the percentage gradually reaches to 62.6, 67.1, 72.6, 79.2, and 84.8% at 0.2, 0.3, 0.5, 1.0, and 2.0 mV·s^{-1}, respectively, as summarized in Figure 6f, which further expounds the reason for the outstanding rate capability property.

With the purpose of clarifying the specific mechanisms and electrochemical products of $MoSe_2$@5%rGO for the Na- and K-ion storage, the electrode materials at the fully discharged/charged positions were studied via *ex situ* measurements. The TEM image at the first full insertion state of Na ion in Figure S19a reveals that the generated nanoparticles are still tightly bound to the surface of rGO, meaning that the chemical bonds between $MoSe_2$ and rGO promote excellent structural stability. Figure 7a depicts the corresponding SAED pattern, which can be assigned to (200), (311), (400), (422), (511), and (440) planes of the cubic Na_2Se phase. The HRTEM image in Figure 7b not only indicates the size of a nanoparticle around 3−5 nm but also demonstrates the obvious lattice fringes with spacings of 3.38 and 2.01 Å attributable to (200) and (311) planes, respectively. After the first full extraction of the Na ion, the electrode preserves great integrity with the regenerated active material anchored on rGO in Figure S19b, whose SAED pattern (Figure 7c) is assigned to the hexagonal $MoSe_2$ structure, and the HRTEM image (Figure 7d) displays the (103) plane with an interplanar distance of 2.36 Å, uncovering admirable electrochemical reversibility. For the K-ion storage, the similar nanoparticles confined into the graphene substrate can be evidently observed in Figure S20a after the initial discharge, while a novel K_5Se_3 discharge product with (620) and (411) planes of the tetragonal structure is confirmed in Figure S20b, and a clear (620) plane with a distance of 2.05 Å can be found from the HRTEM image (Figure S20c). As exhibited in Figure S20d,e, the morphology and hexagonal $MoSe_2$ phase are recovered when further charging to 3.0 V, which is also proved by the (103) plane with a lattice spacing of 2.33 Å from the HRTEM result (Figure S20f).

Figure 7e presents the fitting Mo 3d spectra at different conditions. The Mo^{4+} $3d_{3/2}$ and Mo^{4+} $3d_{5/2}$ peaks completely disappear, and the couples of Mo^{6+} become much stronger than the original one at the discharged state, and the emergence of Mo^{6+} is owing to the oxidation of Mo by air, representing that there is a reduction reaction from Mo^{4+} to Mo metal accompanied by Na-ion intercalation.[31] After the Na-ion deintercalation process, the peaks associated with Mo^{4+} appear again, which discloses a highly reversible charge/discharge process. Surprisingly, it is verified by the Mo 3d (Figure 7e) and C 1s (Figure 7f) spectra that the C−Mo and C−O−Mo bonds always exist during the charge/discharge process, which play an important part in sustaining the morphological and structural stability. In the high-resolution Mo 3d fitting spectra of $MoSe_2$@5%rGO for PIBs (Figure S21a), only a pair of peaks for Mo^{6+} at K-ion insertion state can be seen, and the couples of Mo^{4+} $3d_{3/2}$ and Mo^{4+} $3d_{5/2}$ are back at the extraction state, suggesting that a reversible redox behavior of Mo^{4+} ↔ Mo occurs during the K-ion storage process. However, the peaks related to C−Mo vanish at both states, which is caused by larger volume expansion from K-ion insertion compared with that of the Na ion. Most noteworthy is that the press cannot break the robust C−O−Mo bond between $MoSe_2$ and graphene in Figure S21b, which still ensures the integrity and reversibility.

At present, the studies on electrochemical mechanism of $MoSe_2$ for Na-ion storage are consistent, while the discharge product for PIBs is controversial between K_2Se and K_5Se_3.[27,36] According to our CV results and *ex situ* analyses, both

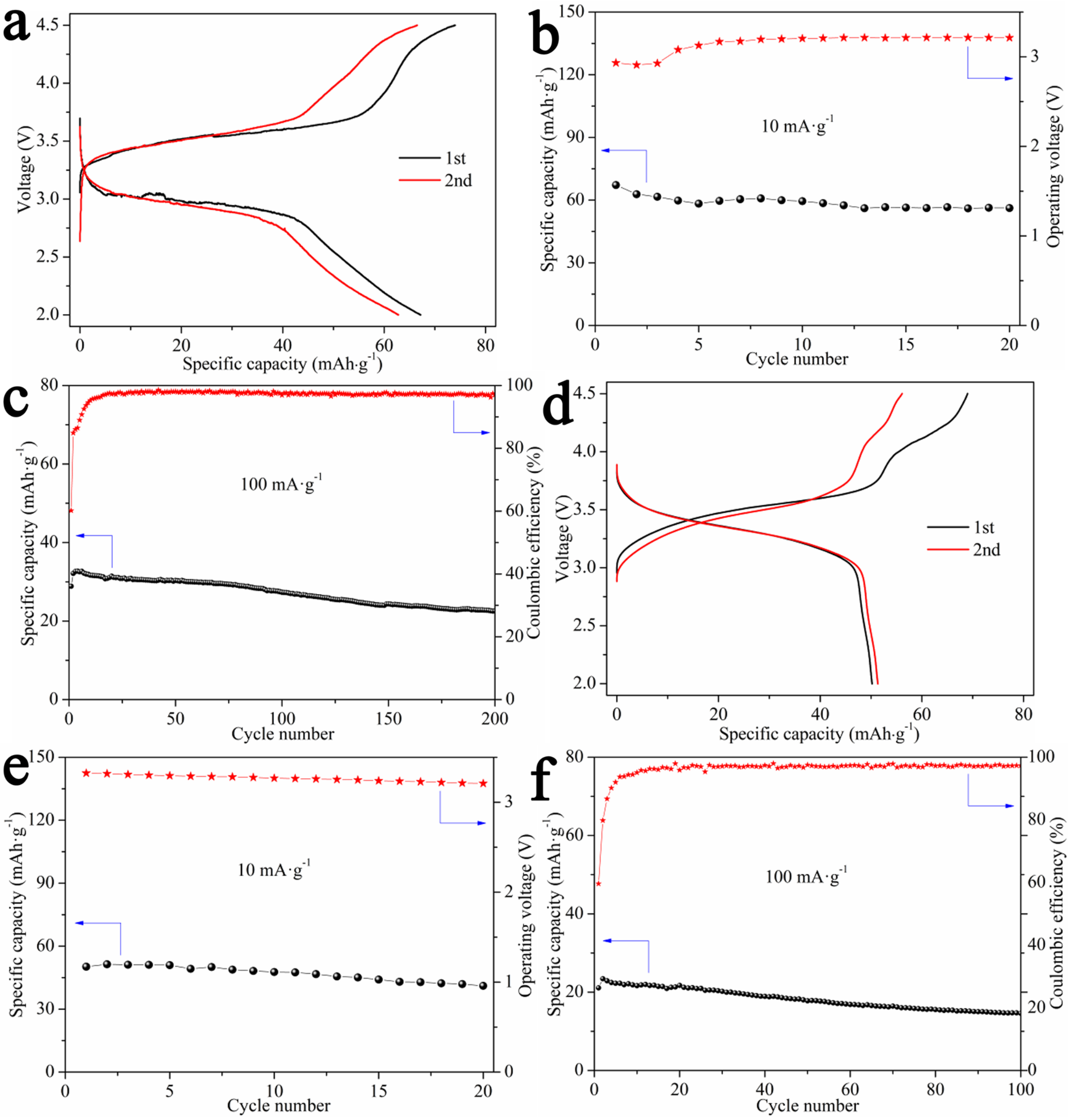

Figure 8. Na- and K-ion full cells with a $Na_2Ni[Fe(CN)_6]$ or $K_2Ni[Fe(CN)_6]$ cathode and $MoSe_2$@5%rGO anode: (a) charge/discharge curves and (b) cycling property at 10 $mA \cdot g^{-1}$, and (c) cycling performance at 100 $mA \cdot g^{-1}$ for SIBs; (d) charge/discharge profiles and (e) cycling curve at 10 $mA \cdot g^{-1}$, and (f) cycling property at 100 $mA \cdot g^{-1}$ for PIBs.

intercalation and conversion mechanisms happen for SIBs and PIBs, whose electrochemical process can be summarized as follows:

SIBs:

$$MoSe_2 + xNa^+ + xe^- \leftrightarrow Na_xMoSe_2, \tag{5}$$

$$Na_xMoSe_2 + (4 - x)Na^+ + (4 - x)e^- \leftrightarrow Mo + 2Na_2Se. \tag{6}$$

PIBs:

$$MoSe_2 + xK^+ + xe^- \leftrightarrow K_xMoSe_2, \tag{7}$$

$$3K_xMoSe_2 + (10 - 3x)K^+ + (10 - 3x)e^- \leftrightarrow 3Mo + 2K_5Se_3. \tag{8}$$

$MoSe_2$ can vertically grow on the surface of the graphene nucleation substrate to form a developed honeycomb-like hierarchical architecture for $MoSe_2$@rGO composite instead of agglomerating into spherical nanoflower morphology for bare $MoSe_2$. First, the constructed hierarchical architecture can decrease the diffusion path of Na and K ions, and the enlarged interplanar spacing will enhance the alkaline ion transport kinetics behavior. Second, the introduction of graphene can not only greatly improve the transfer capability of both ion and electron but also restrain the volume expansion by inhibiting the nanosheet agglomeration and regarding as a buffer region. Third, the formed strong chemical bonds of C−Mo and C−O−Mo between graphene and $MoSe_2$ are beneficial to maintaining the morphological and structural stability during the charge/discharge process. These desirable features are integrated into $MoSe_2$@rGO composite to acquire higher capacity and more superior cycling stability and rate performances compared with the pristine $MoSe_2$.

For the purpose of demonstrating the practical applicability of the $MoSe_2$@5%rGO anode, the Na- and K-ion full batteries were fabricated using $Na_2Ni[Fe(CN)_6]$ and $K_2Ni[Fe(CN)_6]$ cathode electrodes, and the schematic is presented in Figure S22. The electrochemical properties of both cathodes for Na- and K-ion half cells are exhibited in Figure S23 and Figure S24, respectively. The anode electrode was discharged to 0.01 V with metallic sodium/potassium to be inserted enough Na/K ions before fabricating the full battery. Figure 8a gives the charge/discharge curves of the Na-ion full cell with characteristic redox plateaus, showing a first specific capacity of 67.2 $mAh·g^{-1}$ with a working voltage of 2.93 V and an energy density of 196.9 $Wh·kg^{-1}$ at 10 $mA·g^{-1}$. As revealed in Figure 8b, a reversible capacity retention of 56.2 $mAh·g^{-1}$ can be maintained after 20 cycles. The Na-ion full battery also displays long cycling lifetime over 200 cycles with a low capacity fading rate of 0.109% per cycle at 100 $mA·g^{-1}$ in Figure 8c. The K-ion full cell delivers a first capacity of 50.2 $mAh·g^{-1}$ and a voltage of 3.32 V with distinct redox platforms at 10 $mA·g^{-1}$ in Figure 8d, contributing an energy density of 166.7 $Wh·kg^{-1}$. After 20 cycles, the K-ion full cell displays a high retention value of 41.1 $mAh·g^{-1}$ and great voltage stability in Figure 8e. Also, great cycling stability is achieved over 100 cycles at 100 $mA·g^{-1}$ in Figure 8f.

4. CONCLUSIONS

$MoSe_2$@rGO composites assembled by ultrathin $MoSe_2$ nanosheets vertically confined into a graphene substrate, which are prepared via a simple hydrothermal strategy, are reported as anode electrodes for both SIBs and PIBs. The synthesized $MoSe_2$@5%rGO displays much better electrochemical performances than pristine $MoSe_2$, displaying a high specific capacity of 458.3 $mAh·g^{-1}$ at 100 $mA·g^{-1}$, great cyclic stability with a capacity of 383.6 $mAh·g^{-1}$ over 50 cycles, and superior rate capacity of 251.3 $mAh·g^{-1}$ at 5 $A·g^{-1}$ for Na-ion storage. For PIBs, the initial specific capacity of 365.5 $mAh·g^{-1}$ at 100 $mA·g^{-1}$, sustaining the capacity of 314.0 $mAh·g^{-1}$ after 50 cycles, and enhanced rate property (155.2 $mAh·g^{-1}$ at 1 $A·g^{-1}$) are obtained for $MoSe_2$@10%rGO. The great electrochemical performances can be attributed to the hierarchical $MoSe_2$@rGO architecture with a strong interface skeleton connection by chemical bonds of C−Mo and C−O−Mo, and expanded interlayer distance of 7.9 Å, which gives rise to much faster electron transport and alkaline ion diffusion capability as well as more superior structure stability to accommodate the volume expansion. Alkaline ion storage proceeds via continuous reactions of intercalation and conversion with the insertion products of Na_2Se for SIBs and K_5Se_3 for PIBs, respectively, and much better properties for SIBs than PIBs is attributed to more excellent dynamic behavior and double chemical bond stabilization effect. The Na- and K-ion full batteries are also successfully fabricated using $Na_2Ni[Fe(CN)_6]$ and $K_2Ni[Fe(CN)_6]$ cathodes, exhibiting good electrochemical properties.

■ ASSOCIATED CONTENT

Supporting Information

The Supporting Information is available free of charge at https://pubs.acs.org/doi/10.1021/acsami.0c22430.

Additional SEM images, TEM image, HRTEM image, EDS mapping images, SAED pattern, XRD patterns, Raman spectra, N_2 adsorption−desorption isotherms, mesoporous size distribution curves, XPS survey spectra, CV profiles and charge/discharge curves for SIBs, comparison of the rate properties of the previously reported $MoSe_2$-based materials for SIBs with our work, charge/discharge profiles at different current densities for SIBs, CV profiles and charge/discharge curves for PIBs, CV curves at various scanning rates for PIBs, EIS results, TEM images at different states for SIBs and PIBs, SAED patterns, HRTEM images and XPS spectra at the first fully discharged and charged states for PIBs, and illustration diagram of full batteries, as well as charge/discharge curves and cycling stability of $Na_2Ni[Fe(CN)_6]$ and $K_2Ni[Fe(CN)_6]$ cathodes in half cell systems (PDF)

■ AUTHOR INFORMATION

Corresponding Authors

Shaokun Chong − *Frontiers Science Center for Flexible Electronics, Xi'an Institute of Flexible Electronics and Xi'an Institute of Biomedical Materials & Engineering, Northwestern Polytechnical University, Xi'an 710072, PR China;* orcid.org/0000-0002-1931-1779; Email: iamskchong@nwpu.edu.cn

Guozhong Cao − *Department of Materials and Engineering, University of Washington, Seattle, Washington 98195-2120, United States;* orcid.org/0000-0001-6539-0490; Email: gzcao@uw.edu

Wei Huang − *Frontiers Science Center for Flexible Electronics, Xi'an Institute of Flexible Electronics and Xi'an Institute of Biomedical Materials & Engineering, Northwestern Polytechnical University, Xi'an 710072, PR China;* orcid.org/0000-0001-7004-6408; Email: iamwhuang@nwpu.edu.cn

Authors

Xuedong Wei − *Key Laboratory of Magnetic Molecules & Magnetic Information Materials Ministry of Education, School of Chemistry & Material Science, Shanxi Normal University, Linfen 041004, PR China*

Yifang Wu − *Northwest Institute for Nonferrous Metal Research, Xi'an 710016, PR China*

Lan Sun − *State Key Laboratory for Mechanical Behavior of Materials, School of Material Science and Engineering, Xi'an Jiaotong University, Xi'an 710049, PR China*

Chengyong Shu − *School of Chemical Engineering and Technology, Xi'an Jiaotong University, Xi'an 710049, PR China;* orcid.org/0000-0001-8010-6646

Qianbo Lu − *Frontiers Science Center for Flexible Electronics, Xi'an Institute of Flexible Electronics and Xi'an Institute of Biomedical Materials & Engineering, Northwestern Polytechnical University, Xi'an 710072, PR China*

Yingzhen Hu − *Frontiers Science Center for Flexible Electronics, Xi'an Institute of Flexible Electronics and Xi'an Institute of Biomedical Materials & Engineering, Northwestern Polytechnical University, Xi'an 710072, PR China*

Complete contact information is available at: https://pubs.acs.org/10.1021/acsami.0c22430

Notes

The authors declare no competing financial interest.

■ ACKNOWLEDGMENTS

This work was supported by the financial support from the Fundamental Research Funds for the Central Universities (grant G2020KY0534), the National Natural Science Foundation of China (grant 51901187), and the Natural Science Basic Research Program of Shaanxi (grant 2019JQ-612).

■ REFERENCES

(1) Dunn, B.; Kamath, H.; Tarascon, J.-M. Electrical Energy Storage for the Grid: A Battery of Choices. *Science* **2011**, *334*, 928−935.

(2) Wu, X.; Leonard, D. P.; Ji, X. Emerging Non-Aqueous Potassium-Ion Batteries: Challenges and Opportunities. *Chem. Mater.* **2017**, *29*, 5031−5042.

(3) Wang, C.-Y.; Zhang, G.; Ge, S.; Xu, T.; Ji, Y.; Yang, X.-G.; Leng, Y. Lithium-Ion Battery Structure that Self-Heats at Low Temperatures. *Nature* **2016**, *529*, 515−518.

(4) Chong, S.; Chen, Y.; Yan, W.; Guo, S.; Tan, Q.; Wu, Y.; Jiang, T.; Liu, Y. Suppressing Capacity Fading and Voltage Decay of Li-Rich Layered Cathode Material by A Surface Nano-Protective Layer of CoF_2 for Lithium-Ion Batteries. *J. Power Sources* **2016**, *332*, 230−239.

(5) Larcher, D.; Tarascon, J.-M. Towards Greener and More Sustainable Batteries for Electrical Energy Storage. *Nat. Chem.* **2015**, *7*, 19−29.

(6) Xiang, X.; Zhang, K.; Chen, J. Recent Advances and Prospects of Cathode Materials for Sodium-Ion Batteries. *Adv. Mater.* **2015**, *27*, 5343−5364.

(7) Zhang, W.; Liu, Y.; Guo, Z. Approaching High-Performance Potassium-Ion Batteries via Advanced Design Strategies and Engineering. *Sci. Adv.* **2019**, *5*, No. eaav7412.

(8) Huang, Y.; Zheng, Y.; Li, X.; Adams, F.; Luo, W.; Huang, Y.; Hu, L. Electrode Materials of Sodium-Ion Batteries toward Practical Application. *ACS Energy Lett.* **2018**, *3*, 1604−1612.

(9) Kim, H.; Ji, H.; Wang, J.; Ceder, G. Next-Generation Cathode Materials for Non-Aqueous Potassium-Ion Batteries. *Trends Chem.* **2019**, *1*, 682−692.

(10) Chong, S.; Wu, Y.; Guo, S.; Liu, Y.; Cao, G. Potassium Nickel Hexacyanoferrate as Cathode for High Voltage and Ultralong Life Potassium-Ion Batteries. *Energy Storage Mater.* **2019**, *22*, 120−127.

(11) Chong, S.; Yang, J.; Sun, L.; Guo, S.; Liu, Y.; Liu, H. K. Potassium Nickel Iron Hexacyanoferrate as Ultra-Long-Life Cathode Material for Potassium-Ion Batteries with High Energy Density. *ACS Nano* **2020**, *14*, 9807−9818.

(12) Fan, L.; Ma, R.; Zhang, Q.; Jia, X.; Lu, B. Graphite Anode for A Potassium-Ion Battery with Unprecedented Performance. *Angew. Chem., Int. Ed.* **2019**, *58*, 10500−10505.

(13) Bommier, C.; Ji, X. Recent Development on Anodes for Na-Ion Batteries. *Isr. J. Chem.* **2015**, *55*, 486−507.

(14) Zuo, X.; Zhu, J.; Müller-Buschbaum, P.; Cheng, Y.-J. Silicon Based Lithium-Ion Battery Anodes: A Chronicle Perspective Review. *Nano Energy* **2017**, *31*, 113−143.

(15) Jung, S. C.; Jung, D. S.; Choi, J. W.; Han, Y.-K. Atom-Level Understanding of the Sodiation Process in Silicon Anode Material. *J. Phys. Chem. Lett.* **2014**, *5*, 1283−1288.

(16) Lee, S.; Jung, S. C.; Han, Y.-K. First-Principles Molecular Dynamics Study on Ultrafast Potassium Ion Transport in Silicon Anode. *J. Power Sources* **2019**, *415*, 119−125.

(17) Tian, H.; Wang, T.; Zhang, F.; Zhao, S.; Wan, S.; He, F.; Wang, G. Tunable Porous Carbon Spheres for High-Performance Rechargeable Batteries. *J. Mater. Chem. A* **2018**, *6*, 12816−12841.

(18) Chen, J.; Yang, B.; Hou, H.; Li, H.; Liu, L.; Zhang, L.; Yan, X. Disordered, Large Interlayer Spacing, and Oxygen-Rich Carbon Nanosheets for Potassium Ion Hybrid Capacitor. *Adv. Energy Mater.* **2019**, *9*, 1803894.

(19) Zhang, J.; Liu, T.; Cheng, X.; Xia, M.; Zheng, R.; Peng, N.; Yu, H.; Shui, M.; Shu, J. Development Status and Future Prospect of Non-Aqueous Potassium Ion Batteries for Large Scale Energy Storage. *Nano Energy* **2019**, *60*, 340−361.

(20) Wu, C.; Dou, S.-X.; Yu, Y. The State and Challenges of Anode Materials Based on Conversion Reactions for Sodium Storage. *Small* **2018**, *14*, 1703671.

(21) Yu, Q.; Jiang, B.; Hu, J.; Lao, C.-Y.; Gao, Y.; Li, P.; Liu, Z.; Suo, G.; He, D.; Wang, W. A.; Yin, G. Metallic Octahedral $CoSe_2$ Threaded by N-Doped Carbon Nanotubes: A Flexible Framework for High-Performance Potassium-Ion Batteries. *Adv. Sci.* **2018**, *5*, 1800782.

(22) David, L.; Bhandavat, R.; Singh, G. MoS_2/Graphene Composite Paper for Sodium-Ion Battery Electrodes. *ACS Nano* **2014**, *8*, 1759−1770.

(23) Wang, W.; Jiang, B.; Qian, C.; Lv, F.; Feng, J.; Zhou, J.; Wang, K.; Yang, C.; Yang, Y.; Guo, S. Pistachio-Shuck-Like $MoSe_2$/C Core/Shell Nanostructures for High-Performance Potassium-Ion Storage. *Adv. Mater.* **2018**, *30*, 1801812.

(24) Hu, H.; Zhang, J.; Guan, B.; Lou, X. W. D. Unusual Formation of CoSe@Carbon Nanoboxes, Which Have An Inhomogeneous Shell, for Efficient Lithium Storage. *Angew. Chem., Int. Ed.* **2016**, *55*, 9514−9518.

(25) Liu, H.; Guo, H.; Liu, B.; Liang, M.; Lv, Z.; Adair, K. R.; Sun, X. Few-Layer $MoSe_2$ Nanosheets with Expanded (002) Planes Confined in Hollow Carbon Nanospheres for Ultrahigh-Performance Na-Ion Batteries. *Adv. Funct. Mater.* **2018**, *28*, 1707480.

(26) Soares, D. M.; Singh, G. Superior Electrochemical Performance of Layered WTe_2 as Potassium-Ion Battery Electrode. *Nanotechnology* **2020**, *31*, 455406.

(27) Chen, J.; Pan, A.; Wang, Y.; Cao, X.; Zhang, W.; Kong, X.; Su, Q.; Lin, J.; Cao, G.; Liang, S. Hierarchical Mesoporous $MoSe_2$@CoSe/N-Doped Carbon Nanocomposite for Sodium Ion Batteries and Hydrogen Evolution Reaction Applications. *Energy Storage Mater.* **2019**, *21*, 97−106.

(28) Huang, H.; Cui, J.; Liu, G.; Bi, R.; Zhang, L. Carbon-Coated $MoSe_2$/MXene Hybrid Nanosheets for Superior Potassium Storage. *ACS Nano* **2019**, *13*, 3448−3456.

(29) Yousaf, M.; Wang, Y.; Chen, Y.; Wang, Z.; Firdous, A.; Ali, Z.; Mahmood, N.; Zou, R.; Guo, S.; Han, R. P. S. A 3D Trilayered CNT/$MoSe_2$/C Heterostructure with An Expanded $MoSe_2$ Interlayer Spacing for An Efficient Sodium Storage. *Adv. Energy Mater.* **2019**, *9*, 1900567.

(30) Zhao, X.; Cai, W.; Yang, Y.; Song, X.; Neale, Z.; Wang, H.-E.; Sui, J.; Cao, G. $MoSe_2$ Nanosheets Perpendicularly Grown on Graphene with Mo-C Bonding for Sodium-Ion Capacitors. *Nano Energy* **2018**, *47*, 224−234.

(31) Chu, J.; Yu, Q.; Yang, D.; Xing, L.; Lao, C.-Y.; Wang, M.; Han, K.; Liu, Z.; Zhang, L.; Du, W.; Xi, K.; Bao, Y.; Wang, W. A. Thickness-Control of Ultrathin Bimetallic Fe-Mo Selenide@N-Doped Carbon Core/Shell "Nano-Crisps" for High-Performance Potassium-Ion Batteries. *Appl. Mater. Today* **2018**, *13*, 344−351.

(32) Luo, Z.; Zhou, J.; Wang, L.; Fang, G.; Pan, A.; Liang, S. Two-Dimensional Hybrid Nanosheets of Few Layered $MoSe_2$ on Reduced Graphene Oxide as Anodes for Long-Cycle-Life Lithium-Ion Batteries. *J. Mater. Chem. A* **2016**, *4*, 15302−15308.

(33) Liu, H.; Liu, B.; Guo, H.; Liang, M.; Zhang, Y.; Borjigin, T.; Yang, X.; Wang, L.; Sun, X. N-Doped C-Encapsulated Scale-Like Yolk-Shell Frame Assembled by Expanded Planes Few-Layer $MoSe_2$ for Enhanced Performance in Sodium-Ion Batteries. *Nano Energy* **2018**, *51*, 639−648.

(34) Yang, J.; Zhu, J.; Xu, J.; Zhang, C.; Liu, T. $MoSe_2$ Nanosheet Array with Layered MoS_2 Heterostructures for Superior Hydrogen Evolution and Lithium Storage Performance. *ACS Appl. Mater. Interfaces* **2017**, *9*, 44550−44559.

(35) Chong, S.; Sun, L.; Shu, C.; Guo, S.; Liu, Y.; Wang, W. A.; Liu, H. K. Chemical Bonding Boosts Nano-Rose-Like MoS_2 Anchored on Reduced Graphene Oxide for Superior Potassium-Ion Storage. *Nano Energy* **2019**, *63*, 103868.

(36) Ma, K.; Jiang, H.; Hu, Y.; Li, C. 2D Nanospace Confined Synthesis of Pseudocapacitance-Dominated MoS_2-in-Ti_3C_2 Superstructure for Ultrafast and Stable Li/Na-Ion Batteries. *Adv. Funct. Mater.* **2018**, *28*, 1804306.

https://dx.doi.org/10.1021/acsami.0c22430
ACS Appl. Mater. Interfaces 2021, 13, 13158−13169

(37) Ding, Y.-L.; Kopold, P.; Hahn, K.; van Aken, P. A.; Maier, J.; Yu, Y. A Lamellar Hybrid Assembled from Metal Disulfide Nanowall Arrays Anchored on A Carbon Layer: *In Situ* Hybridization and Improved Sodium Storage. *Adv. Mater.* **2016**, *28*, 7774−7782.

(38) Xie, K.; Yuan, K.; Li, X.; Lu, W.; Shen, C.; Liang, C.; Vajtai, R.; Ajayan, P.; Wei, B. Superior Potassium Ion Storage *via* Vertical MoS_2 ″Nano-Rose″ with Expanded Interlayers on Graphene. *Small* **2017**, *13*, 1701471.

(39) Zhao, X.; Sui, J.; Li, F.; Fang, H.; Wang, H.; Li, J.; Cai, W.; Cao, G. Lamellar $MoSe_2$ Nanosheets Embedded with MoO_2 Nanoparticles: Novel Hybrid Nanostructures Promoted Excellent Performances for Lithium Ion Batteries. *Nanoscale* **2016**, *8*, 17902−17910.

(40) Li, J.; Hu, H.; Qin, F.; Zhang, P.; Zou, L.; Wang, H.; Zhang, K.; Lai, Y. Flower-Like $MoSe_2$/C Composite with Expanded (002) Planes of Few-Layer $MoSe_2$ as the Anode for High-Performance Sodium-Ion Batteries. *Chem. − Eur. J.* **2017**, *23*, 14004−14010.

(41) Park, G. D.; Kim, J. H.; Park, S.-K.; Kang, Y. C. $MoSe_2$ Embedded CNT-Reduced Graphene Oxide Composite Microsphere with Superior Sodium Ion Storage and Electrocatalytic Hydrogen Evolution Performances. *ACS Appl. Mater. Interfaces* **2017**, *9*, 10673−10683.

(42) Zhang, Y.; Liu, Z.; Zhao, H.; Du, Y. $MoSe_2$ Nanosheets Grown on Carbon Cloth with Superior Electrochemical Performance as Flexible Electrode for Sodium Ion Batteries. *RSC Adv.* **2016**, *6*, 1440−1444.

(43) Wang, H.; Wang, L.; Wang, X.; Quan, J.; Mi, L.; Yuan, L.; Li, G.; Zhang, B.; Zhong, H.; Jiang, Y. High Quality $MoSe_2$ Nanospheres with Superior Electrochemical Properties for Sodium Batteries. *J. Electrochem. Soc.* **2016**, *163*, A1627−A1632.

(44) Wang, H.; Lan, X.; Jiang, D.; Zhang, Y.; Zhong, H.; Zhang, Z.; Jiang, Y. Sodium Storage and Transport Properties in Pyrolysis Synthesized $MoSe_2$ Nanoplates for High Performance Sodium-Ion Batteries. *J. Power Sources* **2015**, *283*, 187−194.

(45) Ge, J.; Fan, L.; Wang, J.; Zhang, Q.; Liu, Z.; Zhang, E.; Liu, Q.; Yu, X.; Lu, B. $MoSe_2$/N-Doped Carbon as Anodes for Potassium-Ion Batteries. *Adv. Energy Mater.* **2018**, *8*, 1801477.

(46) Gao, H.; Zhou, T.; Zheng, Y.; Zhang, Q.; Liu, Y.; Chen, J.; Liu, H.; Guo, Z. CoS Quantum Dot Nanoclusters for High-Energy Potassium-Ion Batteries. *Adv. Funct. Mater.* **2017**, *27*, 1702634.